LAWRENCE
LIVERMORE
NATIONAL
LABORATORY

LLNL-JRNL-837586

Machine learning reveals key ion selectivity mechanisms in polymeric membranes with sub-nanometer pores

T. A. Pham, H. Kulik, M. Elimelech, C. Ritt, M. Liu, R. Epsztein

July 18, 2022

Science Advances

Disclaimer

Machine learning reveals key ion selectivity mechanisms in polymeric membranes with sub-nanometer pores

Authors

Cody L. Ritt[1], Mingjie Liu[2], Tuan Anh Pham[3], Razi Epsztein[4], Heather J. Kulik[2*], and Menachem Elimelech[1*]

Affiliations

[1]*Department of Chemical and Environmental Engineering, Yale University, New Haven, Connecticut 06520-8286*

[2]*Department of Chemical Engineering, Massachusetts Institute of Technology, Cambridge, Massachusetts 02139*

[3]*Quantum Simulations Group, Lawrence Livermore National Laboratory, Livermore, California 94550*

[4]*Faculty of Civil and Environmental Engineering, Technion – Israel Institute of Technology, Haifa 32000, Israel*

*Corresponding author: Menachem Elimelech, Email: menachem.elimelech@yale.edu, Phone: (203) 432-2789; Heather J. Kulik, Email: hjkulik@mit.edu, Phone: (617) 253-4584

ABSTRACT

Designing single-species selective membranes for high precision separations requires a fundamental understanding of the molecular interactions governing solute transport. Here, we comprehensively assess molecular-level features that influence the separation of 18 different anions by nanoporous cellulose acetate membranes. Our analysis identifies the limitations of bulk solvation characteristics to explain ion transport, highlighted by the poor correlation between hydration energy and the measured permselectivity (R^2 = 0.37). Entropy–enthalpy compensation, spanning 40 kJ mol^{-1}, leads to a free energy barrier ($\Delta G^{\ddagger}$) variation of only ~8 kJ mol^{-1} across all anions. We apply machine learning to elucidate descriptors for energetic barriers from a set of 126 collected features. Notably, electrostatic features account for 75% of the overall features used to describe $\Delta G^{\ddagger}$, despite the relatively uncharged state of cellulose acetate. Our work presents a new approach for studying ion transport across nanoporous membranes that could enable the design of ion-selective membranes.

One Sentence Summary: Machine learning unveils molecular transport mechanisms obscured by entropy-enthalpy compensation in polymeric membranes.

MAIN TEXT

INTRODUCTION

Rapid population growth and industrialization have elicited unprecedented global water and energy demands (*1*). Inextricably linked, water production and energy generation processes could benefit tremendously from the development of separations materials with single-solute selectivity (*2*). Polymeric membranes with sub-nm pores represent a highly practical class of materials for achieving such design goals (*3*). For water treatment purposes, ultra-selective membranes can enable precise control over the makeup of permeate and brine streams for complex feed solutions. This level of control could enable more sustainable water treatment by tailoring the treatment to the desired end use and would significantly reduce chemical and energy consumption, ultimately lowering the treatment cost for water production (*3, 4*). In addition, fit-for-purpose membranes could improve resource recovery efforts (e.g., lithium recovery), sensor devices, and proton selectivity in fuel cells and water electrolyzers (*3*).

Biological channels, like the potassium (K^+) channel, epitomize solute selectivity. By offering a sub-nm environment tailored for K^+, potassium channels can offset the energy-intensive dehydration process induced by extreme confinement, allowing K^+ to transport $>10^4$ faster than similar cations like sodium (Na^+) (*5, 6*). Incorporating ion-selective channels or ligands in polymer matrices to mimic the selective behavior of biological channels has gained recent interest (*7*). This technique remains unproven, however, with experimental performance falling far below conventional polymeric and biological membranes due to fabrication-induced defects (*2, 8*). New and innovative approaches, which require a deeper understanding of fundamental structure–property–performance relationships in polymeric membranes, are thus imperative for designing solute-tailored selectivity.

Various ion-specific properties can influence ion transport, and hence, ion selectivity. The hydration energy (*9-11*), charge density (*12*), and size of an ion have conventionally been considered to play critical roles in ion transport (*9, 12, 13*). The relative importance of each property toward selective transport, however, remains largely clouded. Our poor understanding of the mechanisms that govern ion-ion selectivity in membranes is, in part, the result of inadequate performance metrics. Ion transport in most salt-rejecting membranes is characterized by the observed rejection. Not only is this an operationally dependent metric, but it also fails to capture the thermodynamics necessary for elucidating important molecular interactions (*14*). Additionally, the conventional Edisonian approach to studying selective transport is often incapable of deconvoluting strongly coupled transport mechanisms. This approach largely relies on elucidating

transport phenomena from correlations between ion permeability and singular membrane modifications that are often characterized by only a few physical measurements. The sensitivity of polymeric membranes to their environment, which is evidenced by their anomalous ionization behavior (*15*), as well as the complex, inhomogeneous nature of their cross-linked networks restricts the insight of such analyses.

In this work, we comprehensively assess the role of monovalent anion- and membrane-specific properties in overall salt transport. Our analysis focuses on the separation of a wide array of anions of monovalent sodium-based salts by a nanoporous cellulose acetate (CA) membrane to elucidate phenomenological differences in selectivity originating from the anions. We identify the limited role of bulk solvation characteristics while highlighting the critical need to consider entropic barriers when holistically studying ion transport. We combine our experimental data with properties describing ion and ion-membrane interactions—generated from first-principles simulations in this study and obtained elsewhere—for advanced statistical analysis using machine learning techniques to determine the most important features for predicting thermodynamic barriers to transport. Notably, we observe entropy–enthalpy compensation (EEC) in the transport thermodynamics, largely influenced by ion-membrane interactions under confinement. Although our results are specific to the membrane used in this study, the reported findings demonstrate a new approach for studying ion transport across all nanoporous polymeric membranes.

RESULTS

Bulk ion solvation: An inadequate descriptor for ion-ion selectivity

Partial or complete shedding of an ion's solvation shell—termed 'dehydration'—has been proposed as a universal mechanism for ion selectivity in rigid 2-D nanoporous systems (*16*). Previous studies of nanoporous polymeric systems frequently relate ion hydration energy, ΔG_{Hyd}, which describes the energy released when an ion undergoes solvation (*17*), to the ability of an ion to dehydrate into a confined environment (*10-12*). Hence, ions with high ΔG_{Hyd} are considered to have strong solvation shells that are not easily shed. In other words, ions with high ΔG_{Hyd} incur a substantial energetic penalty for dehydrating, making dehydration unfavorable. The use of ΔG_{Hyd} as a standalone metric for assessing dehydration-limited ion permeation is suspect, however, and has been criticized for its failure to account for other solvation properties that have been shown to influence dehydration, such as the hydrated radius (*18*). Furthermore, the use of ΔG_{Hyd} to explain dehydration-limited transport is often based on the trends of only a select few ions (*19*).

We explore the viability of ΔG_{Hyd} as a rate-limiting property for ion transport by assessing the correlation between ΔG_{Hyd} and water-salt selectivity for 18 different anions (Fig. 1A). The anions

investigated can be found in table S1. We find a positive correlation between ΔG_{Hyd} and permselectivity, suggesting that ΔG_{Hyd} is a possible descriptor for dehydration mechanisms that influence anion permeation. However, the strength of the correlation is poor (R^2 = 0.37). ΔG_{Hyd} therefore cannot be reliably used to describe the rate-limiting step for ion transport. This finding does not discredit the possibility of ion dehydration as a rate-limiting mechanism or bulk solvation properties as adequate descriptors for ion dehydration into membranes. Instead, there may exist other bulk solvation properties that are better proxies for ion dehydration.

The solvated size of an ion is another extensively used bulk solvation property for explaining ion dehydration mechanisms in nanoporous membranes (*12, 13, 16, 20*). Typically represented by the hydrated radius (r_{Hyd}), this property describes the effective size of an ion when considering water molecules electrostatically bound to the ion surface (*17*). The hydrated radius is inextricably linked with ΔG_{Hyd}, but it also includes steric and, to some degree, shape effects. An ion whose solvated size is larger than the membrane pore must at least partially dehydrate to enter, assuming the pore is a rigid structure. While larger ΔG_{Hyd} typically corresponds with larger r_{Hyd}, this is not always the case. The molecular geometry of an ion influences the charge distribution across its surface and consequently the extent to which it can grow its solvation shell.

Anisotropic (i.e., asymmetric) solvation from ordered structuring of water molecules around the more electronegative regions of an ion is inherent to many polyatomic ions and has been identified as critical to ion dehydration (*21*). Anisotropy is not reliably captured by r_{Hyd}, as r_{Hyd} is a time-averaged value estimated for a sphere. Alternatively, the ion-water binding energy (ΔG_B), which describes the interaction strength of a single water molecule with the ion, can be used to characterize the effect of anisotropic ordering on solvation strength (*22*). By applying first-principles molecular dynamics (FPMD) simulations (see Methods) to compute the hydrogen-bonding probability density functions (H-bonding PDFs) between water molecules and ions, we visualize the effect of anisotropic ordering (Fig. 1B-C). Specifically, we compare the two-dimensional (2-D) projection distributions of water hydrogens surrounding Cl^- and ClO^-, which illustrate how non-uniform electrostatic potentials result in the severe asymmetric solvation of ClO^- as water molecules preferentially bind to the oxygen atom (Fig. 1D).

[INSERT FIG. 1]

As evidenced in Fig. 1B-D, anisotropic solvation produces stark differences in the solvated structure of an ion. We thus extend our FPMD simulations to the entire chlorate series (Fig. 2A) to investigate the role of anisotropic solvation in ion selectivity. The bond distance and intensity loosely represent the ion solvation strength. We used the H-bonding PDFs to calculate r_{Hyd}, and we

computed ΔG_B and ΔG_{Hyd} using density functional theory (DFT, see Methods) for chloride (Cl^-), hypochlorite (ClO^-), chlorite (ClO_2^-), chlorate (ClO_3^-), and perchlorate (ClO_4^-), which can be found in Fig. 2B. The trend in simulated ΔG_{Hyd} ($ClO^- > ClO_2^- > Cl^- > ClO_3^- > ClO_4^-$) differs slightly from ΔG_{Hyd} values reported by ref. (*17*), in which the ΔG_{Hyd} of ClO_2^- was larger than ClO^-.

Despite being interrelated properties, the trend for r_{Hyd} ($ClO_4^- > ClO^- > ClO_3^- > ClO_2^- > Cl^-$) differs substantially from that of the simulated ΔG_{Hyd} due to shape effects and ionic size (Fig. 2B). r_{Hyd} can instead be readily described by the number of water molecules that coordinate with the anion (fig. S1A). ΔG_B follows the same trend as ΔG_{Hyd} (fig. S1B), but the two are not perfectly correlated ($R^2 = 0.86$) due to the added influence of anisotropic water ordering present in ΔG_B.

We assess the quality of ΔG_B and r_{Hyd} as rate-limiting predictors for anion permeation by quantifying the change in the fit accuracy (i.e., R^2 value) for permselectivity relative to ΔG_{Hyd} (Fig. 2C). This analysis was only done with the values simulated by FPMD for ions in the chlorate series. We believe the chlorate series is a suitable sample representation for all the anions investigated in this study given its wide breadth of molecular geometries and ΔG_{Hyd}. Using ΔG_B as a predictor improved the fit accuracy by 4.1% relative to ΔG_{Hyd}. This suggests that incorporating anisotropic solvation characteristics may be beneficial when trying to describe dehydration mechanisms with bulk solvation properties. Surprisingly, r_{Hyd}, which has been extensively used to explain dehydration-limited ion transport, was a far worse predictor for permselectivity than ΔG_{Hyd} ($\Delta R^2 =$ –75.4%). Collectively, our analysis highlights that bulk solvation properties are poor descriptors for the rate-limiting step in anion transport across polymeric membranes. This likely stems from the inability of bulk solvation properties to adequately account for extrinsic factors that can influence dehydration, such as compensatory ion-membrane interactions (*3*).

[ISNERT FIG. 2]

Energetic barriers: The critical role of entropy

The inability of bulk solvation properties to describe anion permselectivity or dehydration necessitates a more fundamental thermodynamic view of transport (thermodynamic parameters detailed in table S2). Ion solvation in water is enthalpically favorable and entropically unfavorable (*17*). The process of dehydration is therefore often thought to take the reverse. However, this logic fails to consider the confined system that the ion is dehydrating into. While removing an ion from bulk water increases the entropy of water, previous theoretical work has observed a corresponding decrease in the system's entropy as the ion permeates the channel—making entropy the major contributor to the permeation barrier (*23*). A balance is also often struck between entropy and enthalpy for steric and diffusive hindrance factors (discussion in Supplementary Materials, fig. S2).

We approximate the energetics of dehydration into our nanoporous membrane for several anions (Fig. 3A). This is accomplished with empirically-derived equations (*17*) that estimate the transfer energy ($\Delta_t G^\infty$) and enthalpy ($\Delta_t H^\infty$) associated with ions dehydrating into a non-aqueous solvent (details in Supplementary Materials, fig. S3). Given the dramatic change in the physical and electrical properties of water confined below 2 nm (*24, 25*), we can assume that confined water represents a non-aqueous solvent (table S3). Our results indicate that entropic barriers play a predominant role in dehydration as they account for over half of $\Delta_t G^\infty$ for all anions examined except thiocyanate (SCN^-). Entropy should thus be accounted for if dehydration, and the energetics thereof, are to be considered rate-limiting mechanisms for anion permeation. We also find that uncommonly used ionic properties for interpreting ion dehydration, such as molar refractivity and softness, may influence dehydration (details in Supplementary Materials, table S4 and fig. S4).

Our analysis suggests that enthalpy alone cannot reasonably describe anion dehydration, partitioning, or diffusion processes. This explains the limited success and inconsistencies associated with using activation energy, E_a, as a descriptor for transport (fig. S5) (*12*), which is directly related to enthalpy (*26*). We therefore applied transition state theory (TST) to relate water-salt selectivity to the free energy barrier, $\Delta G^\ddagger$ (see Methods). While our measurements are of the entire salt, relative changes in $\Delta G^\ddagger$ are solely attributable to the anion due to all salts being sodium-based (*27*). To utilize Eq. 2, which links TST to diffusive permeation (*26*), we isolated the role of advective transport (details in Supplementary Materials, figs. S6-9). Although present, advection (i.e., ion transport mediated by fluid flow) did not influence differences in anion permselectivity or $\Delta G^\ddagger$ (figs. S8-9).

The intrinsic correlation between permselectivity and $\Delta G^\ddagger$, which spans from 34.2 to 42.5 kJ mol^{-1} (Fig. 3B), allows us to reliably extract meaningful entropic, $T\Delta S^\ddagger$, and enthalpic, $\Delta H^\ddagger$, barriers for anion permeation (Fig. 3C). Notably, $\Delta G^\ddagger$ does not mirror $\Delta_t G^\infty$. This suggests that dehydration does not solely govern ion transport in this system, which is likely due to an observed entropy–enthalpy compensation (EEC) effect: anions with high entropic barriers (i.e., more negative $T\Delta S^\ddagger$) experience relatively small enthalpic resistance, and vice versa. EEC is a common occurrence in selective ion-ligand association (*28, 29*). Enthalpically-favorable ion-membrane interactions can help reduce $\Delta G^\ddagger$ (*3*). However, these interactions are met with a corresponding loss of entropy in the form of reduced degrees of translational and rotational freedom (*28*). This tradeoff likely gives rise to the EEC observed in Fig. 3C, which is, to the best of our knowledge, the first report of EEC for ion transport across membranes.

[INSERT FIG. 3]

Relative role of molecular-level features in transport

Describing ion transport holistically necessitates multiple feature types that capture all relevant ion and ion-membrane interaction properties. We obtained feature data from: (1) DFT calculations conducted in this study (see Methods), (2) cheminformatics (CI) descriptors from the open-source toolkit, RDKit (*30*), and (3) previously published works. DFT calculations and CI descriptors inform the electronic and structural properties of the ion, respectively. DFT is further extended to compute interaction properties between the ion and the membrane material. Macroscopic properties collected from previously published work include commonly used variables important to transport, such as the diffusion coefficient (*26*), that may not be adequately described by DFT or CI. This extensive data collection resulted in 126 features (tables S5-8) that were classified into eight qualitative categories related to ion or ion-membrane interaction properties (Fig. 4A). Categorical mapping was designed to highlight the collective role of strongly interrelated properties and avoid overinterpreting the physical meaning of individual features selected for a small sample set (*31, 32*).

The linear regression models were trained for $\Delta H^{\ddagger}$, $T\Delta S^{\ddagger}$, and $\Delta G^{\ddagger}$ (Fig. 4B-D). Feature-selected subsets were obtained with Recursive Feature Addition (RFA, see Methods). The low mean absolute errors (MAEs < 10%) from RFA are a significant improvement over those obtained from the regularized linear regression (see Methods) used for comparison. The MAE for the $\Delta G^{\ddagger}$ model (Fig. 4D) is almost twofold larger than the MAEs for the $T\Delta S^{\ddagger}$ and $\Delta H^{\ddagger}$ models. This is largely due to the outlier, tetrafluoroborate (BF_4^-). Removing BF_4^- would decrease the MAE of the $\Delta G^{\ddagger}$ model to 3.71%. BF_4^- may behave as an outlier due to its anomalous chemical behavior (*33*). This could also likely be due to poor extrapolation by the $\Delta G^{\ddagger}$ model given BF_4^- has the lowest $\Delta G^{\ddagger}$ value (34.23 kJ mol^{-1}). Nonetheless, the decent predictive capability of the models indicate that model feature importance is predictive of design principles.

Both $T\Delta S^{\ddagger}$ and $\Delta H^{\ddagger}$ rely strongly on the absolute coefficients (β) from ion structure, accounting for 21.1 and 30.2% of the total feature importance, respectively (Fig. 4E-F). Macroscopic features selected for $T\Delta S^{\ddagger}$ (e.g., molecular weight) are also highly correlated with ion structure, increasing the cumulative role of ion structure in $T\Delta S^{\ddagger}$ to 38.2%. Ion-membrane interactions under confinement are the most important feature category for $T\Delta S^{\ddagger}$ ($\beta / \sum \beta$ = 45.3%). The outsized importance of interaction properties corroborates our physical interpretation of EEC—favorable interactions between the ion and CA coincide with entropy loss from reduced degrees of freedom in the membrane. This effect is compounded by the ionic structure, whose shape and size can further complicate the ion's ability to contort and translate across the dense polymer network (*14*).

Cumulative ion-membrane interaction properties (i.e., interaction properties in bulk, under confinement, and those from macroscopic features) are also found to be important for $\Delta H^{\ddagger}$ ($\beta / \sum \beta$ = 27.3%). The parallelism between $T\Delta S^{\ddagger}$ and $\Delta H^{\ddagger}$ model features corresponds to the EEC effect observed in Fig. 3C. However, $\Delta H^{\ddagger}$ is influenced by ion polarizability ($\beta / \sum \beta$ = 36.1%) substantially more than $T\Delta S^{\ddagger}$ is ($\beta / \sum \beta$ = 6.5%). The selection of ion polarizability indicates that dehydration mechanisms are important as ion polarizability indirectly describes an ion's response to the environment permittivity and its ability to dehydrate into other media (additional discussion in Supplementary Materials) (*17*). It has also been shown previously that this parameter is paramount for understanding ion transport across organic–water interfaces (*34*). The shedding and reorganization of water molecules during dehydration or binding interactions has been suggested as a ubiquitous source for EEC in water-mediated processes (*35*).

The apparent equivalence of the EEC tradeoff results in an almost net-neutral output, where $\Delta G^{\ddagger}$ varies by only ~8 kJ mol^{-1} despite $T\Delta S^{\ddagger}$ and $\Delta H^{\ddagger}$ each spanning a range of roughly 40 kJ mol^{-1} between all anions (Fig. 3B-C). Similar EEC behavior has been observed in biomolecular ligand recognition (*29*). This behavior, sometimes termed the "window effect," may be the consequence of the transport process having a finite heat capacity and could explain the limited role of interaction properties in determining overall ion transport (Fig. 4G) (*36*). Ion electrostatics are instead the most important feature category for $\Delta G^{\ddagger}$ ($\beta / \sum \beta$ = 75.3%). Although the anions studied here possess the same formal charge, the importance of electrostatics in ion selectivity may stem from the influence of non-uniform charge distributions across polyatomic ions, which are critical to molecular interactions, such as hydrogen bonding or dehydration (*21, 37*). Confined ion-membrane interactions and polarizability account for 19.7% and 4.9% of the total feature importance, respectively. The strong correlation between $\Delta G^{\ddagger}$ and permselectivity (Fig. 3B) signifies that these features are critical for distinguishing anions during selective transport. Notably, bulk solvation properties were not selected as important features for $\Delta G^{\ddagger}$ (table S9). Our model correctly predicts a higher $\Delta G^{\ddagger}$ for ClO_3^- compared to Cl^- due to the greater electrostatic potential variance across the surface of ClO_3^-. This counters expectations from previous interpretations on the role of bulk ion solvation in transport (*9-12*), which would predict a higher $\Delta G^{\ddagger}$ for Cl^- corresponding to its larger hydration energy.

[INSERT FIG. 4]

DISCUSSION

Despite recent optimism surrounding the use of TST to understand the molecular mechanisms of solute transport in membranes from an entropy and enthalpy perspective (*3*), we find that EEC may limit this possibility. Entropy and enthalpy are intricately intertwined. The compensation between the two can complicate the interpretation of thermodynamic signatures, consequently obscuring the physics underlying the observed data (*29*). Therefore, determining the appropriate membrane modifications and design approach to tailor ion selectivity is not straightforward. Previous studies have called for using insight from EEC to guide ligand design (*38, 39*), but this strategy has demonstrated limited utility (*29*). Our results show that designing membrane channels and matrices from a free energy perspective is more suitable for achieving ion selectivity in nanoporous membranes.

Further, we find there are more important components that influence free energy barriers during ion permeation. In particular, the relationship between the pore and the ion electrical properties are critically important, despite the relatively uncharged nature of the CA membrane (*40*). The implications of this finding may extend to membrane design. Given the observed importance of electrostatics for predicting $\Delta G^{\ddagger}$, we postulate that increasing the charge density of the membrane may enhance its ion-ion selectivity. This relies on the assumption that increasing the charge density would not substantially alter the steric environment of the membrane via excessive swelling. However, a trade-off between ion-ion selectivity and charge density likely exists, as was found between water-salt selectivity and charge density in nanoporous polyamide membranes (*15*).

We interpolated a monovalent anion not used in the training set (azide, N_3^-) to further assess the predictability of the $\Delta G^{\ddagger}$ model. The predicted $\Delta G^{\ddagger}$ (36.45 kJ mol^{-1}) and permselectivity (P_W/P_S = 91) for N_3^- coincide extraordinarily well with its measured values: 36.51 ± 0.26 kJ mol^{-1} and 92 ± 9, respectively (table S10). This finding corroborates the predictability implied by its low MAE and suggests our model successfully captures the critical features for differentiating monovalent anion transport. We extended our interpolation to sulfate (SO_4^{2-}) to assess the model's predictability beyond monovalent anions. The predicted $\Delta G^{\ddagger}$ of SO_4^{2-} (36.56 kJ mol^{-1}) suggests that SO_4^{2-} should be able to permeate the CA membrane more readily than Cl^- ($\Delta G^{\ddagger}$ = 37.76 kJ mol^{-1}). However, this is counter to experimental observations, which show SO_4^{2-} rejection significantly higher than Cl^- in nanoporous CA membranes (*41*). Unsurprisingly, this signifies that the model can interpolate well but struggles to extrapolate to new trends it has not yet seen. Adding data for divalent ions will extend the promise of this approach by providing key features that are likely necessary for comparing transport between ions of varying valency, such as the total valence or charge density.

The results and data produced herein are specific to the nanoporous cellulose acetate membrane investigated in this study. Nonetheless, our findings show that advanced statistical techniques and machine learning can be applied to elucidate molecular mechanisms that govern selective ion transport. Such techniques allow for incorporating a wide array of variables rather than focusing on a readily available few. This approach can also provide more insight into the nature of selective transport in complex environments, such as highly cross-linked and inhomogeneous polymer membranes. Our findings represent an essential step toward the ability to design membranes with ultrahigh ion selectivity.

MATERIALS AND METHODS

Materials and chemicals

A CK-series commercial cellulose acetate (CA) NF membrane (GE Osmonics, Minnetonka, MN), with a reported molecular weight cut-off (MWCO) of ~2000 Da was used for filtration tests. To abate experimental variation from roll-to-roll processing variability, all CA membranes tested in this study were produced from the same batch (Lot #3CK00009). The membranes were received as flat sheet samples and were gently washed with deionized (DI) water to remove any preservatives. Membranes were stored in DI water at 4 °C. All sodium-based monovalent salts (≥ 99%) used for anion rejection tests were purchased from Sigma-Aldrich (St. Louis, MO).

Membrane characterization

The average pore size of the NF membrane was estimated by the hindered transport model, which accounts for steric exclusion as well as hindered convection and diffusion of neutral organic solutes (*42*). We employed erythritol, xylose, and dextrose (≥ 99%, Sigma-Aldrich, St. Louis, MO) as neutrally charged, low molecular weight organic tracers (*43*). Prior to testing, CA membranes were compacted in DI water under 12.1 bar of hydraulic pressure for 12 h. After compaction, 50 mg L^{-1} as total organic carbon (TOC) of the organic solute was circulated in the membrane system. Permeate samples were collected at 1.38, 4.14, 6.89, and 9.65 bar applied pressure with a crossflow velocity of 21.4 cm s^{-1} and feed solution temperature of 25.0 ± 0.5 °C (fig. S10A). The permeate samples were taken after the system was allowed to equilibrate for 30 min at each pressure. Solute rejection was determined by analyzing permeate and feed samples for TOC (TOC V-CSH, Shimadzu Corp., Kyoto, Japan). Further details on the pore size estimation can be found in the Supplementary Materials.

The asymmetric structure of the membrane cross-sections was characterized by scanning electron microscopy (SEM, SU-70, 5 kV, Hitachi, Tokyo, Japan) (fig. S10B). Samples were sputter

coated with 2 nm of iridium (208HR Sputter Coater, Cressington, Watford, UK) to improve sample conductivity during SEM. Images were captured at 1,200× magnification.

Nanofiltration system and anion rejection experiments

A custom-built 3-cell bench-scale filtration system operating in crossflow mode with a flat sheet membrane cell was used for salt rejection and water permeability tests (fig. S11). The crossflow velocity and effective membrane surface area were 21.4 cm s^{-1} and 20.0 cm^2, respectively. Retentate and permeate were recirculated between the feed tank and the membrane cells. Prior to filtration experiments, membranes were compacted in DI water under 12.1 bar of hydraulic pressure for 12 h. Unless stated otherwise, all filtration experiments were performed with an applied inlet pressure of 6.89 bar to avoid compaction effects that may influence membrane performance. Pure water permeability was determined with only DI water circulating in the system. The feed solution temperature was kept constant at 22.0 ± 0.5 °C during compaction and pure water filtration experiments. Feed solution temperature was varied for anion rejection experiments from 16 to 34 ± 0.5 °C at 6 °C increments. All experiments were operated at pH 5.8, excluding those conducted with sodium hypochlorite (NaOCl) and sodium bicarbonate ($NaHCO_3$). Filtration experiments with NaOCl and $NaHCO_3$ were carried out at pH 9 and pH 8.4, respectively, to ensure monovalent anionic speciation. Permeate and feed samples were collected after the system was allowed to equilibrate for 30 min.

Observed salt rejection (R_{obs}) was determined by comparing the salt concentration in the feed (C_f) and permeate (C_p) solutions ($R_{obs} = 1 - C_p/ C_f$). We used a C_f of 2 mmol L^{-1} for all filtration experiments. Salt flux (J_S, mol m^{-2} h^{-1}) across the membrane was determined by coupling the measured water flux (J_W, L m^{-2} h^{-1}) with C_p ($J_S = J_W C_p$). By considering the concentration difference across the membrane, we can extract the salt permeability coefficient, B (L m^{-2} h^{-1}), from the relation $B = J_S / \Delta C_m$. Here, ΔC_m is the difference in the salt concentration between the permeate and feed-side membrane surface, which can be determined by accounting for concentration polarization in the diffusive boundary layer (details in Supplementary Materials).

The intrinsic water/salt permselectivity (P_W/P_S) is an inherent material property (i.e., it is operation independent) that was used to compare the ability of the membrane to discriminate the various ions investigated in this study (*4, 40*):

$$\frac{P_W}{P_S} = \frac{R_g T}{\hat{V}_W} \frac{R_o \exp\left(\frac{J_W}{k_{sol}}\right)}{(1-R_o)\left[\Delta P - \Delta\pi \exp\left(\frac{J_W}{k_f}\right)\right]} \quad (1)$$

where R_g, T, and $\hat{V}_W$ are the ideal gas constant (83.145 cm^3 bar K^{-1} mol^{-1}), absolute temperature (298.15 K), and molar volume of water (18 cm^3 mol^{-1}), respectively. The driving force is described by the difference between the applied hydraulic pressure (ΔP, bar) and transmembrane osmotic pressure ($\Delta\pi$, bar). A value of 100 L m^{-2} h^{-1} was assumed for the overall feed-side mass transfer coefficient (k_f) and the feed-side mass transfer coefficient for the solute of interest (k_{sol}) (*4*).

Measurement of anion transport energetics

Transport energy barriers were assessed using transition state theory (TST), which describes a rate constant (k, s^{-1}) in terms of entropic ($\Delta S^{\ddagger}$) and enthalpic ($\Delta H^{\ddagger}$) barriers (i.e., activation energies) and can be extended to solute permeability (*3, 26, 44*):

$$k = B\left(\frac{\delta}{\lambda_m{}^2}\right) = \kappa\frac{k_B T}{h}\exp\left(\frac{\Delta S^{\ddagger}}{R}\right)\exp\left(\frac{\Delta H^{\ddagger}}{RT}\right) \quad (2)$$

where δ is the membrane thickness (m), λ_m is the average distance between energy minima (m) as permeating molecules hop between sites within the membrane (details in Supplementary Materials), κ is the transmission coefficient (assumed as unity) (*44*), k_B is the Boltzmann constant (1.381×10^{-23} J K^{-1}), and h is the Planck constant (6.626×10^{-23} J s). The entropic barriers are accessible by taking the y-intercept of the linearized form of Eq. 2 (*3*). Similarly, enthalpic barriers are determined from the slope of the linearized equation and can be related, in principle, to the Arrhenius activation energy, E_a, by a factor of RT (i.e., $E_a = \Delta H^{\ddagger} + RT$) (*26*).

First-principles molecular dynamics (FPMD) simulations

We carried out FPMD simulations to probe the bulk solvation properties of ions in the chlorate series. Specifically, all solutions were modeled by periodic cubic cells consisting of 63 water molecules and a single solvated ion, with the excess charge compensated by a uniform background charge. The size of the cells was chosen to yield the experimental density of liquid water under ambient conditions. The simulations were carried out using Born–Oppenheimer MD with the Qbox code (*45*), with the interatomic force derived from DFT and the Perdew, Burke, and Ernzerhof approximation for the exchange-correlation energy functional (*46*). The interaction between valence electrons and ionic cores was represented by norm-conserving pseudopotentials (*47*), and the electronic wave functions were expanded in a plane-wave basis set truncated at a cutoff energy of 85 Ry. All hydrogen atoms were replaced with deuterium to maximize the allowable time step, which was chosen to be 10 atomic units. The equilibration runs were carried out at an elevated temperature of T = 400 K to recover the experimental water structure and diffusion, while also providing a good description of the ion solvation at room temperature (*48*). For the analysis of

structural properties, the statistics were collected over 45 ps microcanonical simulations after an equilibration run of 15 ps.

Based on the simulations, we evaluated the strength of the hydration shell of the anions (E_{sol}) using cluster calculations. Specifically, E_{sol} was approximated as the binding energy of the ion–water clusters, $X^-(H_2O)_n$, where X^- corresponds to the anions and n is the number of water molecules in the first ion solvation shell. Here, the strength of the ion hydration shell is estimated as $E_{sol} = E(X^-(H_2O)_n) - E(X^-) - E((H_2O)_n)$, where $E(X^-(H_2O)_n)$, $E((H_2O)_n)$, and $E(X^-)$ are the energies of the $X^-(H_2O)_n$ and $(H_2O)_n$ clusters, and the ion X^- in vacuum, respectively. The calculation was carried out with a uniform positive background charge to neutralize the system, with Markov–Payne correction to account for spurious interactions between periodic images (*49*). The final values of E_{sol} were obtained by averaging the results over 500 configurations of $X^-(H_2O)_n$ clusters extracted directly from the corresponding simulations. For each cluster, the number of water molecules was determined using the distance cutoff as the first minimum of the ion–oxygen radial distribution functions (RDFs) of the ions. This distance cutoff represents the hydrated radius of the ion.

Property curation and feature selection models

We collected ionic properties and descriptors from previously published work (table S5), information extracted from ion SMILES strings in the RDKit package (*50-52*) (table S6), and DFT simulations conducted herein (tables S7-8). DFT simulations were performed with a developmental version of GPU-accelerated TeraChem v1.9 (*53, 54*). The B3LYP (*55-57*) global hybrid functional with semi-empirical D3 dispersion correction (*58-61*) was employed with an LANL2DZ (*62*) effective core potential basis set for heavy atoms (i.e., Br, I, and Mn) and the 6-31G* basis for all other atoms. Relative properties of the ions are expected to be insensitive to this functional/basis set choice. For isolated ion calculations, properties (table S7) were computed in both the gas phase and a dielectric approximating water in bulk ($\varepsilon = 78$) and under confinement ($\varepsilon = 30$) (*63*) using the C-PCM solvation model (*64, 65*), as implemented in TeraChem (*53, 54*). The cluster of the CA unit structure was modeled to study the interaction between ions and the CA (fig. S7). To ensure we sample equivalent CA effects for each ion, geometry optimizations of ions are carried out with the CA fixed. The initial positions of the ions are only considered over the acetyl groups and the tetrahydropyran rings, which carry the most negative and positive charges, respectively, and are therefore assumed to represent the most and the least favorable binding sites for the anions (fig. S7). Ion-CA interaction properties (table S7) were obtained under two dielectric constant environments to represent interactions in bulk water ($\varepsilon = 78$) and under confinement ($\varepsilon = 30$) (*63*), similar to the isolated ion calculations.

Recursive Feature Addition (RFA) that adds features sequentially to the target model (*66*) to eliminate less informative features was used for building the linear regression model for all the properties. The models are judged by Leave-One-Out Cross Validation (LOOCV) (*67*), and the mean absolute error (MAE) is used to estimate the model's performance. Consistent with a typical RFA approach, at each iteration, the linear regression model implemented in scikit-learn (*68*) is trained with a new feature set, and a descriptor is kept only if adding the new feature yields a decrease in the MAE of >1% (fig. S12). For the selected subset of features, the feature importance is ranked by the absolute coefficient in the linear regression model (table S9). The absolute coefficient determined for each feature is obtained by averaging the absolute coefficients of the 18 linear regression models generated during LOOCV. We also evaluate the L1-regularized, least absolute shrinkage and selection operator (LASSO) linear least-square regression (*69*) to train the model for feature selection as implemented in scikit-learn (*68*). The regularization hyperparameter λ was obtained with grid search in the range [1e-8, 1e-4]. The optimized hyperparameters, MAE, and two model's performance comparison for target properties are compared in table S11.

SUPPLEMENTARY MATERIALS

Supplementary material for this article is available at URL

REFERENCES AND NOTES

1. P. D'Odorico, K. F. Davis, L. Rosa, J. A. Carr, D. Chiarelli, J. Dell'Angelo, J. Gephart, G. K. MacDonald, D. A. Seekell, S. Suweis, M. C. Rulli, The global food-energy-water nexus. *Rev. Geophys.* **56**, 456-531 (2018).
2. S. K. Patel, C. L. Ritt, A. Deshmukh, Z. Wang, M. Qin, R. Epsztein, M. Elimelech, The relative insignificance of advanced materials in enhancing the energy efficiency of desalination technologies. *Energy Environ. Sci.* **13**, 1694-1710 (2020).
3. R. Epsztein, R. M. DuChanois, C. L. Ritt, A. Noy, M. Elimelech, Towards single-species selectivity of membranes with subnanometre pores. *Nat. Nanotechnol.* **15**, 426-436 (2020).
4. J. R. Werber, A. Deshmukh, M. Elimelech, The critical need for increased selectivity, not increased water permeability, for desalination membranes. *Environ. Sci. Technol. Lett.* **3**, 112-120 (2016).
5. Y. F. Zhou, J. H. Morais-Cabral, A. Kaufman, R. MacKinnon, Chemistry of ion coordination and hydration revealed by a K^+ channel-Fab complex at 2.0 Å resolution. *Nature* **414**, 43-48 (2001).
6. D. A. Doyle, J. M. Cabral, R. A. Pfuetzner, A. L. Kuo, J. M. Gulbis, S. L. Cohen, B. T. Chait, R. MacKinnon, The structure of the potassium channel: Molecular basis of K^+ conduction and selectivity. *Science* **280**, 69-77 (1998).
7. R. Sujanani, M. R. Landsman, S. Jiao, J. D. Moon, M. S. Shell, D. F. Lawler, L. E. Katz, B. D. Freeman, Designing solute-tailored selectivity in membranes: Perspectives for water reuse and resource recovery. *ACS Macro Lett.* **9**, 1709-1717 (2020).
8. C. J. Porter, J. R. Werber, M. Zhong, C. J. Wilson, M. Elimelech, Pathways and challenges

for biomimetic desalination membranes with sub-nanometer channels. *ACS Nano* **14**, 10894-10916 (2020).
9. B. Tansel, Significance of thermodynamic and physical characteristics on permeation of ions during membrane separation: Hydrated radius, hydration free energy and viscous effects. *Sep. Purif. Technol.* **86**, 119-126 (2012).
10. B. Tansel, J. Sager, T. Rector, J. Garland, R. F. Strayer, L. F. Levine, M. Roberts, M. Hummerick, J. Bauer, Significance of hydrated radius and hydration shells on ionic permeability during nanofiltration in dead end and cross flow modes. *Sep. Purif. Technol.* **51**, 40-47 (2006).
11. L. A. Richards, B. S. Richards, B. Corry, A. I. Schafer, Experimental energy barriers to anions transporting through nanofiltration membranes. *Environ. Sci. Technol.* **47**, 1968-1976 (2013).
12. R. Epsztein, E. Shaulsky, N. Dizge, D. M. Warsinger, M. Elimelech, Role of ionic charge density in donnan exclusion of monovalent anions by nanofiltration. *Environ. Sci. Technol.* **52**, 4108-4116 (2018).
13. L. A. Richards, A. I. Schafer, B. S. Richards, B. Corry, The importance of dehydration in determining ion transport in narrow pores. *Small* **8**, 1701-1709 (2012).
14. W. J. Koros, C. Zhang, Materials for next-generation molecularly selective synthetic membranes. *Nat. Mater.* **16**, 289-297 (2017).
15. C. L. Ritt, J. Werber, M. Wang, Z. Yang, Y. Zhao, H. J. Kulik, M. Elimelech, Ionization behavior of nanoporous polyamide membranes. *Proc. Natl. Acad. Sci. U.S.A.* **117**, 30191-30200 (2020).
16. S. Sahu, M. Di Ventra, M. Zwolak, Dehydration as a universal mechanism for ion selectivity in graphene and other atomically thin pores. *Nano Lett.* **17**, 4719-4724 (2017).
17. Y. Marcus, *Ions in solution and their solvation*. (John Wiley & Sons, Inc., Hoboken, New Jersey, 2015).
18. R. C. Smith, P. Mukherjee, A. K. SenGupta, Comment on "Experimental energy barriers to transporting anions through nanofiltration membranes". *Environ. Sci. Technol.* **47**, 8985-8986 (2013).
19. R. Epsztein, E. Shaulsky, M. Qin, M. Elimelech, Activation behavior for ion permeation in ion-exchange membranes: Role of ion dehydration in selective transport. *J. Membr. Sci.* **580**, 316-326 (2019).
20. J. Abraham, K. S. Vasu, C. D. Williams, K. Gopinadhan, Y. Su, C. T. Cherian, J. Dix, E. Prestat, S. J. Haigh, I. V. Grigorieva, P. Carbone, A. K. Geim, R. R. Nair, Tunable sieving of ions using graphene oxide membranes. *Nat. Nanotechnol.* **12**, 546-550 (2017).
21. F. Aydin, M. R. Ceron, S. A. Hawks, D. I. Oyarzun, C. Zhan, T. A. Pham, M. Stadermann, P. G. Campbell, Selectivity of nitrate and chloride ions in microporous carbons: The role of anisotropic hydration and applied potentials. *Nanoscale* **12**, 20292-20299 (2020).
22. F. Aydin, C. Zhan, C. Ritt, R. Epsztein, M. Elimelech, E. Schwegler, T. A. Pham, Similarities and differences between potassium and ammonium ions in liquid water: A first-principles study. *Phys. Chem. Chem. Phys.* **22**, 2540-2548 (2020).
23. G. Portella, J. S. Hub, M. D. Vesper, B. L. de Groot, Not only enthalpy: Large entropy contribution to ion permeation barriers in single-file channels. *Biophys. J.* **95**, 2275-2282 (2008).
24. M. Neek-Amal, F. M. Peeters, I. V. Grigorieva, A. K. Geim, Commensurability effects in viscosity of nanoconfined water. *ACS Nano* **10**, 3685-3692 (2016).
25. L. Fumagalli, A. Esfandiar, R. Fabregas, S. Hu, P. Ares, A. Janardanan, Q. Yang, B. Radha, T. Taniguchi, K. Watanabe, G. Gomila, K. S. Novoselov, A. K. Geim, Anomalously low dielectric constant of confined water. *Science* **360**, 1339-1342 (2018).
26. B. J. Zwolinski, H. Eyring, C. E. Reese, Diffusion and membrane permeability. 1. *J. Phys.*

Colloid Chem. **53**, 1426-1453 (1949).
27. X. Zhou, Z. Wang, R. Epsztein, C. Zhan, W. Li, D. Fortner John, A. Pham Tuan, J.-H. Kim, M. Elimelech, Intrapore energy barriers govern ion transport and selectivity of desalination membranes. *Sci. Adv.* **6**, eabd9045 (2020).
28. U. Ryde, A fundamental view of enthalpy-entropy compensation. *Medchemcomm* **5**, 1324-1336 (2014).
29. J. D. Chodera, D. L. Mobley, Entropy-enthalpy compensation: Role and ramifications in biomolecular ligand recognition and design. *Annu. Rev. Biophys.* **42**, 121-142 (2013).
30. G. Landrum, Rdkit: Open-source cheminformatics. http://www.rdkit.org (2006). Accessed December 10, 2020.
31. A. Nandy, J. Zhu, J. P. Janet, C. Duan, R. B. Getman, H. J. Kulik, Machine learning accelerates the discovery of design rules and exceptions in stable metal–oxo intermediate formation. *ACS Catalysis* **9**, 8243-8255 (2019).
32. S. M. Moosavi, A. Nandy, K. M. Jablonka, D. Ongari, J. P. Janet, P. G. Boyd, Y. Lee, B. Smit, H. J. Kulik, Understanding the diversity of the metal-organic framework ecosystem. *Nat. Commun.* **11**, 4068 (2020).
33. S. J. Grabowski, Hydrogen bonds with BF_4^- anion as a proton acceptor. *Crystals* **10**, 460 (2020).
34. C. D. Wick, I. F. W. Kuo, C. J. Mundy, L. X. Dang, The effect of polarizability for understanding the molecular structure of aqueous interfaces. *J. Chem. Theory Comput.* **3**, 2002-2010 (2007).
35. R. Lumry, S. Rajender, Enthalpy–entropy compensation phenomena in water solutions of proteins and small molecules: A ubiquitous property of water. *Biopolymers* **9**, 1125-1227 (1970).
36. A. Cooper, C. M. Johnson, J. H. Lakey, M. Nöllmann, Heat does not come in different colours: Entropy–enthalpy compensation, free energy windows, quantum confinement, pressure perturbation calorimetry, solvation and the multiple causes of heat capacity effects in biomolecular interactions. *Biophys. Chem.* **93**, 215-230 (2001).
37. J. S. Murray, P. Politzer, The electrostatic potential: An overview. *Wiley Interdiscip. Rev. Comput. Mol. Sci.* **1**, 153-163 (2011).
38. G. G. Ferenczy, G. M. Keseru, Thermodynamics guided lead discovery and optimization. *Drug Discov. Today* **15**, 919-932 (2010).
39. J. E. Ladbury, G. Klebe, E. Freire, Adding calorimetric data to decision making in lead discovery: A hot tip. *Nat. Rev. Drug Discov.* **9**, 23-27 (2010).
40. G. M. Geise, D. R. Paul, B. D. Freeman, Fundamental water and salt transport properties of polymeric materials. *Prog. Polym. Sci.* **39**, 1-42 (2014).
41. Y. He, G. M. Li, H. Wang, Z. W. Jiang, J. F. Zhao, H. X. Su, Q. Y. Huang, Experimental study on the rejection of salt and dye with cellulose acetate nanofiltration membrane. *J. Taiwan Inst. Chem. Eng.* **40**, 289-295 (2009).
42. L. D. Nghiem, A. I. Schafer, M. Elimelech, Removal of natural hormones by nanofiltration membranes: Measurement, modeling, and mechanisms. *Environ. Sci. Technol.* **38**, 1888-1896 (2004).
43. M. Xie, L. D. Nghiem, W. E. Price, M. Elimelech, Relating rejection of trace organic contaminants to membrane properties in forward osmosis: Measurements, modelling and implications. *Water Res.* **49**, 265-274 (2014).
44. M. Sogami, S. Era, M. Murakami, Y. Seo, H. Watari, N. Uyesaka, Application of the transition state theory to water transport across cell membranes. *Biochim. Biophys. Acta Biomembr.* **1511**, 42-48 (2001).
45. F. Gygi, Architecture of Qbox: A scalable first-principles molecular dynamics code. *IBM J. Res. Dev.* **52**, 137-144 (2008).

46. J. P. Perdew, K. Burke, M. Ernzerhof, Generalized gradient approximation made simple. *Phys. Rev. Lett.* **77**, 3865-3868 (1996).
47. M. Schlipf, F. Gygi, Optimization algorithm for the generation of ONCV pseudopotentials. *Comput. Phys. Commun.* **196**, 36-44 (2015).
48. T. A. Pham, T. Ogitsu, E. Y. Lau, E. Schwegler, Structure and dynamics of aqueous solutions from PBE-based first-principles molecular dynamics simulations. *J. Chem. Phys.* **145**, (2016).
49. G. Makov, M. C. Payne, Periodic boundary conditions in *ab initio* calculations. *Phys. Rev. B* **51**, 4014-4022 (1995).
50. D. Weininger, SMILES, a chemical language and information system. 1. Introduction to methodology and encoding rules. *J. Chem. Inf. Comput. Sci.* **28**, 31-36 (1988).
51. D. Weininger, SMILES. 3. DEPICT. Graphical depiction of chemical structures. *J. Chem. Inf. Comput. Sci.* **30**, 237-243 (1990).
52. D. Weininger, A. Weininger, J. L. Weininger, SMILES. 2. Algorithm for generation of unique SMILES notation. *J. Chem. Inf. Comput. Sci.* **29**, 97-101 (1989).
53. I. S. Ufimtsev, T. J. Martinez, Quantum chemistry on graphical processing units. 3. Analytical energy gradients, geometry optimization, and first principles molecular dynamics. *J. Chem. Theory Comput.* **5**, 2619-2628 (2009).
54. F. Liu, N. Luehr, H. J. Kulik, T. J. Martínez, Quantum chemistry for solvated molecules on graphical processing units using polarizable continuum models. *J. Chem. Theory Comput.* **11**, 3131-3144 (2015).
55. C. Lee, W. Yang, R. G. Parr, Development of the Colle-Salvetti correlation-energy formula into a functional of the electron density. *Phys. Rev. B* **37**, 785-789 (1988).
56. K. Raghavachari, Perspective on "Density functional thermochemistry. III. The role of exact exchange". *Theor. Chem. Acc.* **103**, 361-363 (2000).
57. P. J. Stephens, F. J. Devlin, C. F. Chabalowski, M. J. Frisch, *Ab initio* calculation of vibrational absorption and circular dichroism spectra using density functional force fields. *J. Phys. Chem.* **98**, 11623-11627 (1994).
58. E. R. Johnson, A. D. Becke, A post-Hartree–Fock model of intermolecular interactions. *J. Chem. Phys.* **123**, 024101 (2005).
59. E. R. Johnson, A. D. Becke, A post-Hartree-Fock model of intermolecular interactions: Inclusion of higher-order corrections. *J. Chem. Phys.* **124**, 174104 (2006).
60. A. D. Becke, E. R. Johnson, A density-functional model of the dispersion interaction. *J. Chem. Phys.* **123**, 154101 (2005).
61. S. Grimme, J. Antony, S. Ehrlich, H. Krieg, A consistent and accurate *ab initio* parametrization of density functional dispersion correction (DFT-D) for the 94 elements H-Pu. *J. Chem. Phys.* **132**, 154104 (2010).
62. P. J. Hay, W. R. Wadt, *Ab initio* effective core potentials for molecular calculations. Potentials for the transition metal atoms Sc to Hg. *J. Chem. Phys.* **82**, 270-283 (1985).
63. A. Friebe, W. Moritz, Influence of electrolyte on electrical-properties of thin cellulose-acetate membranes. *J. Appl. Polym. Sci.* **51**, 625-634 (1994).
64. D. M. York, M. Karplus, A smooth solvation potential based on the conductor-like screening model. *J.Phys. Chem. A* **103**, 11060-11079 (1999).
65. A. W. Lange, J. M. Herbert, A smooth, nonsingular, and faithful discretization scheme for polarizable continuum models: The switching/Gaussian approach. *J. Chem. Phys.* **133**, 244111 (2010).
66. I. Guyon, A. Elisseeff, An introduction to variable and feature selection. *J. Mach. Learn. Res.* **3**, 1157-1182 (2003).
67. C. Sammut, G. I. Webb, "Leave-one-out cross-validation" in *Encyclopedia of machine learning*. (Springer US, Boston, MA, 2010), pp. 600-601.

68. F. Pedregosa, G. Varoquaux, A. Gramfort, V. Michel, B. Thirion, O. Grisel, M. Blondel, P. Prettenhofer, R. Weiss, V. Dubourg, J. Vanderplas, A. Passos, D. Cournapeau, M. Brucher, M. Perrot, É. Duchesnay, Scikit-learn: Machine learning in Python. *J. Mach. Learn. Res.* **12**, 2825–2830 (2011).
69. T. Hastie, R. Tibshirani, J. Friedman, *The elements of statistical learning: Data mining, inference, and prediction*. Springer series in statistics (Springer-Verlag, New York, NY, ed. 2, 2009).
70. I. V. Bodrenko, S. Salis, S. Acosta-Gutierrez, M. Ceccarelli, Diffusion of large particles through small pores: From entropic to enthalpic transport. *J. Chem. Phys.* **150**, 211102 (2019).
71. M. Neek-Amal, A. Lohrasebi, M. Mousaei, F. Shayeganfar, B. Radha, F. M. Peeters, Fast water flow through graphene nanocapillaries: A continuum model approach involving the microscopic structure of confined water. *Appl. Phys. Lett.* **113**, 083101 (2018).
72. V. Crupi, S. Interdonato, F. Longo, D. Majolino, P. Migliardo, V. Venuti, New insight on the hydrogen bonding structures of nanoconfined water: A Raman study. *J. Raman Spectrosc.* **39**, 244-249 (2008).
73. R. J. Mashl, S. Joseph, N. R. Aluru, E. Jakobsson, Anomalously immobilized water: A new water phase induced by confinement in nanotubes. *Nano Lett.* **3**, 589-592 (2003).
74. H. Yasuda, C. E. Lamaze, L. D. Ikenberry, Permeability of solutes through hydrated polymer membranes. I. Diffusion of sodium chloride. *Makromol. Chem.* **118**, 19-35 (1968).
75. M. D. Hanwell, D. E. Curtis, D. C. Lonie, T. Vandermeersch, E. Zurek, G. R. Hutchison, Avogadro: An advanced semantic chemical editor, visualization, and analysis platform. *J. Cheminformatics* **4**, 17 (2012).
76. A. Szymczyk, P. Fievet, Investigating transport properties of nanofiltration membranes by means of a steric, electric and dielectric exclusion model. *J. Membr. Sci.* **252**, 77-88 (2005).
77. R. G. Parr, R. A. Donnelly, M. Levy, W. E. Palke, Electronegativity: The density functional viewpoint. *J. Chem. Phys.* **68**, 3801-3807 (1978).
78. T. Lu, F. W. Chen, Multiwfn: A multifunctional wavefunction analyzer. *J. Comput. Chem.* **33**, 580-592 (2012).
79. A. Alparone, Linear and nonlinear optical properties of nucleic acid bases. *Chem. Phys.* **410**, 90-98 (2013).
80. H. Sekino, R. J. Bartlett, Molecular hyperpolarizabilities. *J. Chem. Phys.* **98**, 3022-3037 (1993).

Acknowledgments

Funding: This work was supported primarily by the Center for Enhanced Nanofluidic Transport, an Energy Frontier Research Center funded by the US Department of Energy, Office of Science, Basic Energy Sciences under Award DE-SC0019112 (experimental work, machine learning, and ion property simulations). Part of this work was performed under the auspices of the U.S. Department of Energy by Lawrence Livermore National Laboratory under Contract DE-AC52-07NA27344 (bulk solvation simulations). We also acknowledge Mengyi Wang for useful discussion during the early stages of the DFT simulations.

Author contributions: C.L.R., R.E., and M.E. designed experimental research; C.L.R. performed experimental research; M.L., T.A.P., and H.J.K. designed and carried out computational research;

C.L.R., M.L., T.A.P., H.J.K., and M.E. analyzed data; C.L.R., M.L., and T.A.P. wrote the paper; and C.L.R., H.J.K., and M.E. edited the manuscript.

Competing interests: The authors declare no competing interests.

Data and materials availability: All data needed to evaluate the conclusions in the paper are present in the paper and/or the Supplementary Materials.

FIGURES AND TABLES

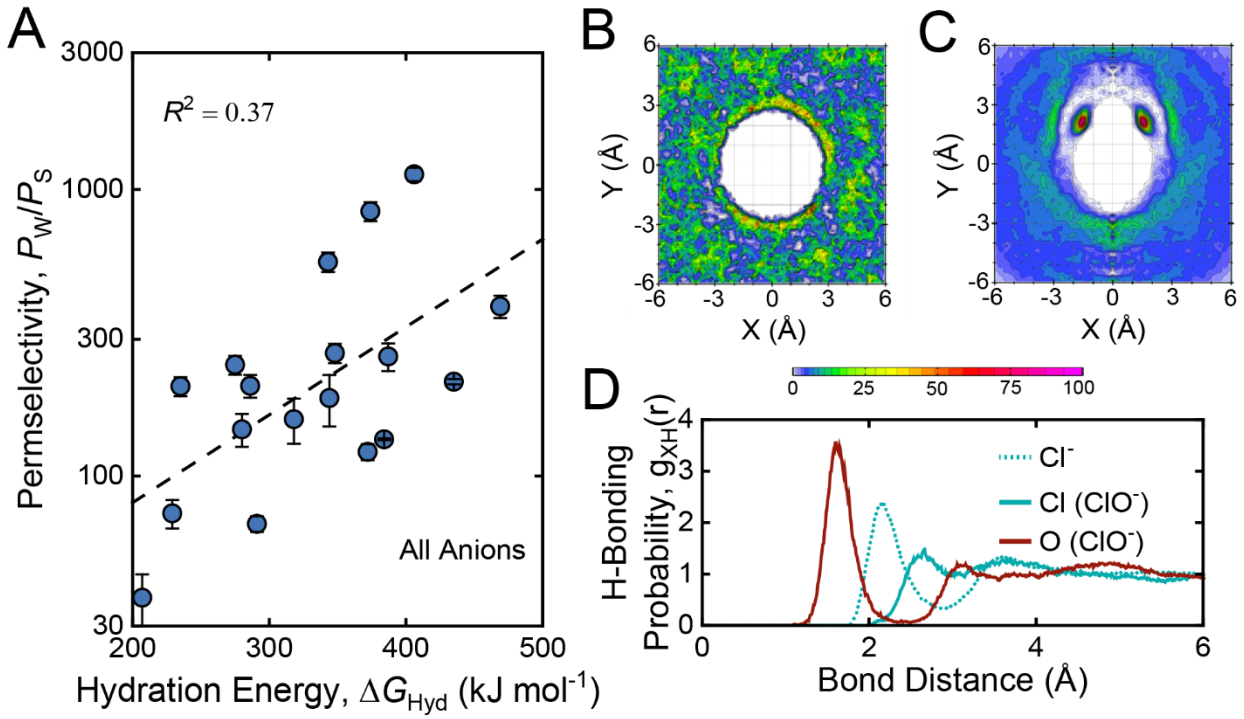

Fig. 1. Assessing bulk ion solvation as a primary metric for ion selectivity in nanoporous membranes. (**A**) Permselectivity of all 18 anions investigated compared to their hydration energies, ΔG_{Hyd} (table S1). All hydration energies used in this analysis were obtained from ref. (*17*). (**B-C**) Two-dimensional projection distributions of water hydrogens surrounding (**B**) chloride, Cl^-, and (**C**) hypochlorite, ClO^-, ions. The scale bar represents the normalized density of water hydrogens, where the values correspond to the percentage probability of finding a hydrogen per nm^2. (**D**) H-bonding probability density functions (PDFs) for Cl^-, and the chlorine (Cl) and oxygen (O) atoms in ClO^-.

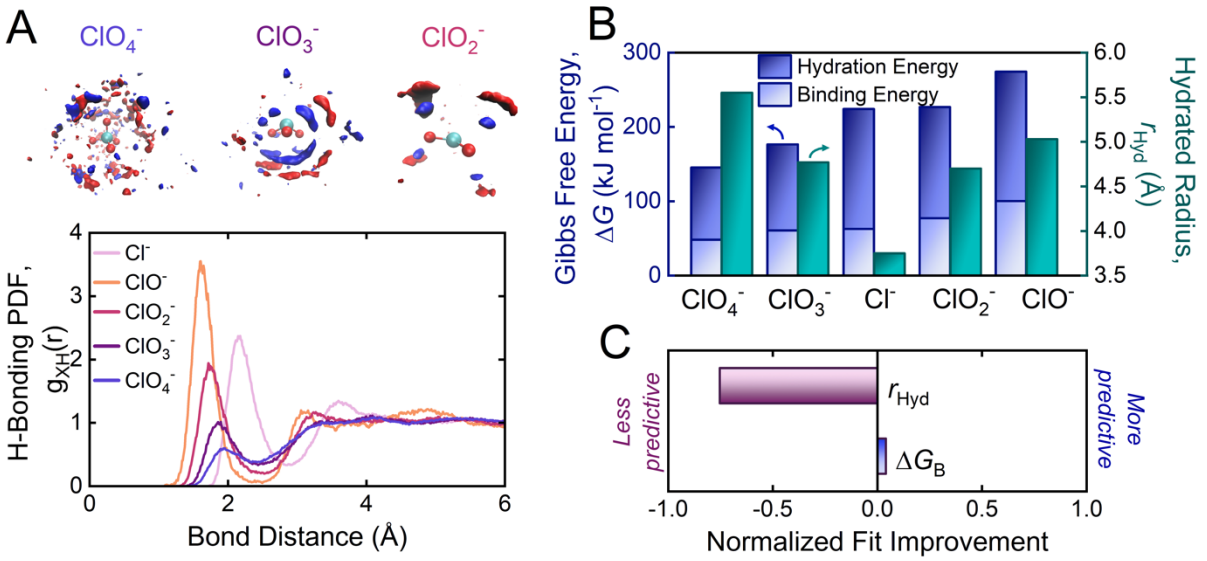

Fig. 2. Role of anisotropic solvation in ion selectivity. (**A**) FPMD simulations of ion solvation. Three-dimensional rendering of solvation shells for several ions in the chlorate series (top) provides a qualitative view of anisotropic ion solvation. Oxygen, hydrogen, and chlorine atoms are represented by red, blue, and cyan colors, respectively. These three-dimensional renderings are based on the probability density function of H-bonds forming between water molecules and the ions of interest (bottom). (**B**) Calculated solvation properties of ions in the chlorate series, determined from FPMD simulations (see Methods). (**C**) Improvement of the linear regression fit—defined as the normalized increase or decrease in the R^2 value from the linear regression with ΔG_{Hyd}—for describing the permselectivity of ions in the chlorate series based on ion-water binding energy (ΔG_B) or r_{Hyd}.

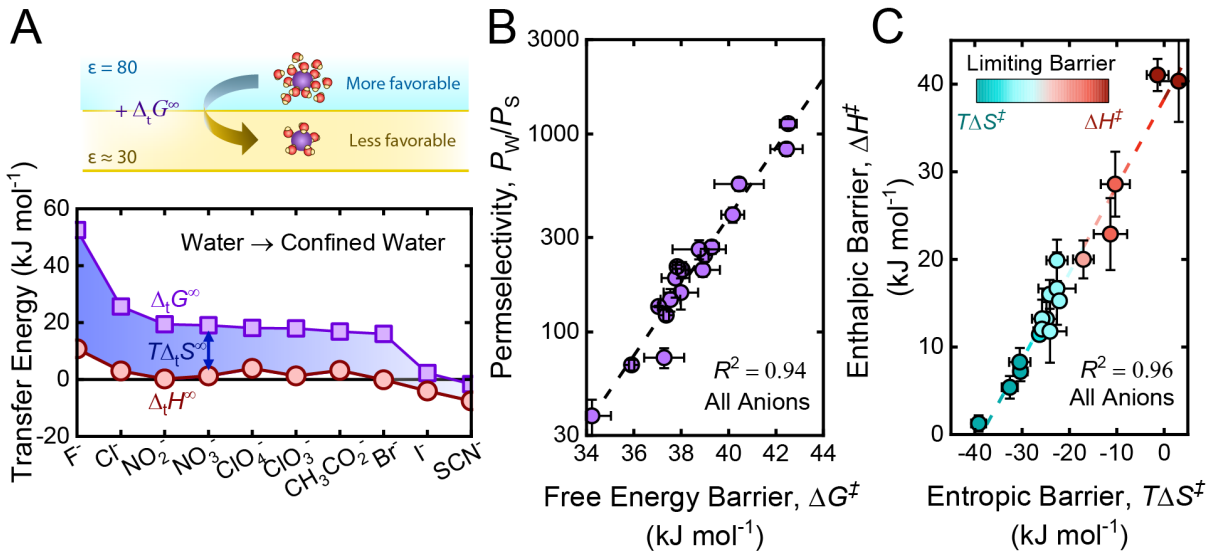

Fig. 3. Role of energetic barriers in ion transport across nanoporous membranes. (**A**) The energetic costs of dehydration into confined water parallels an ion transferring from water to a non-aqueous low-dielectric solvent (top). The free energy and enthalpy for various ions investigated (bottom) illustrates the importance of entropy in the dehydration process. (**B**) Water-salt permselectivity of all 18 anions investigated compared to their measured free energy barriers, $\Delta G^{\ddagger}$, at 22 °C. (**C**) Correlation between measured $\Delta H^{\ddagger}$ and $T\Delta S^{\ddagger}$ for all 18 anions investigated at 22 °C. Datapoints colored cyan and red correspond to entropically- and enthalpically-governed transport, respectively. Error bars represent standard deviations of samples taken in triplicate.

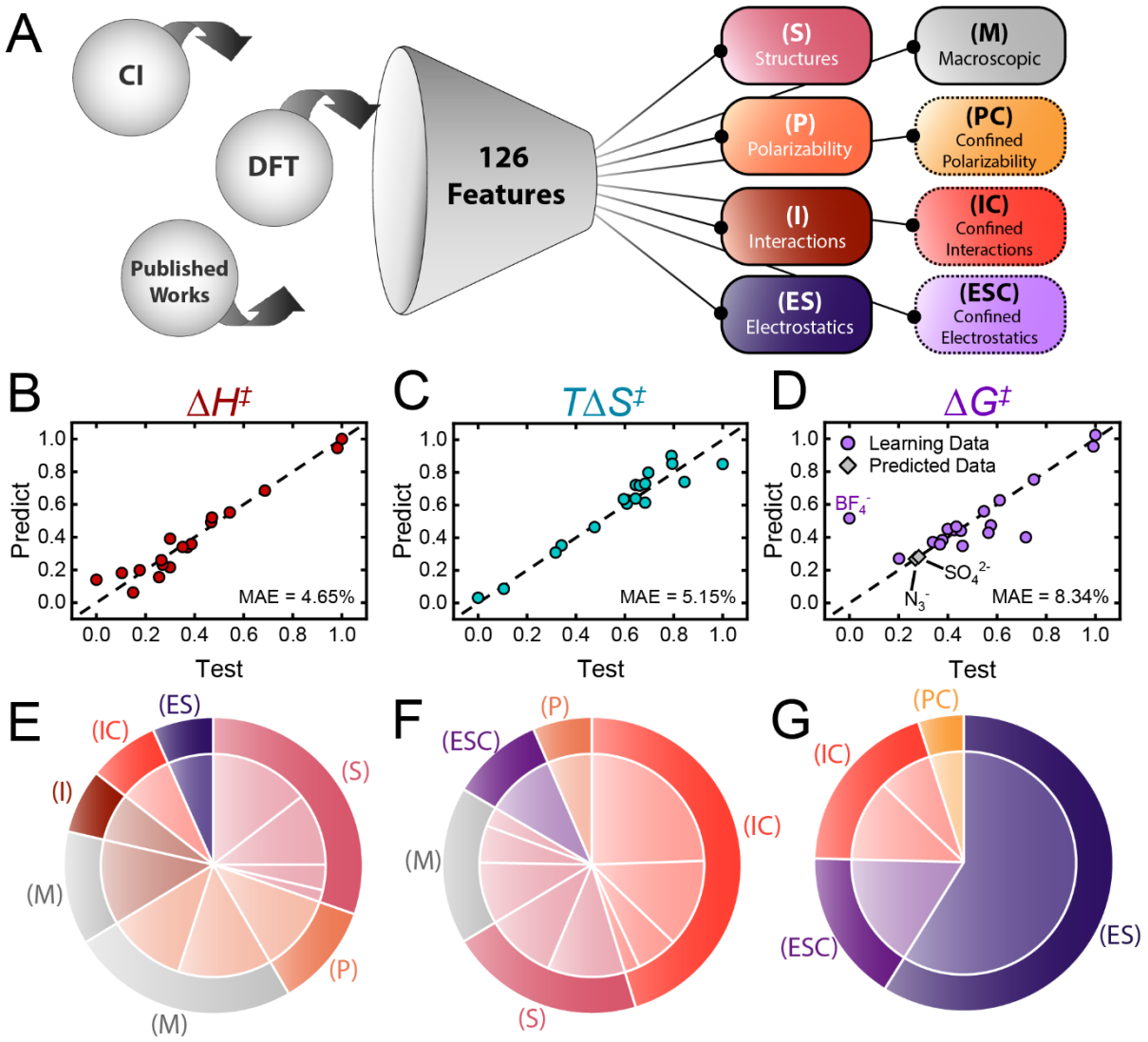

Fig. 4. Elucidating the molecular features that influence anion transport thermodynamics. (**A**) Schematic representation of data sourcing 126 features from cheminformatics (CI), density functional theory (DFT) simulations, and literature (left), and classifying them by qualitative categories related to ion or ion-membrane interaction properties in bulk or confined water (right). Macroscopic properties (M) represent measured values from literature that can indirectly relate to any of the other categories, occasionally overlapping several. (**B-D**) Accuracy of machine learning models for ion (**B**) $\Delta H^{\ddagger}$, (**C**) $T\Delta S^{\ddagger}$, and (**D**) $\Delta G^{\ddagger}$. Accuracy is measured by the mean absolute error (MAE). $\Delta G^{\ddagger}$ predictions for N_3^- and SO_4^{2-} are displayed as grey diamonds in panel d. (**E-G**) Relative makeup (i.e., % contribution) of qualitative feature categories for anion (**E**) $\Delta H^{\ddagger}$, (**F**) $T\Delta S^{\ddagger}$, and (**G**) $\Delta G^{\ddagger}$ models. $\Delta H^{\ddagger}$, $T\Delta S^{\ddagger}$, and $\Delta G^{\ddagger}$ models consist of 11, 11, and 5 total features, respectively. Two "(M)" labels were provided in panel e to highlight that the macroscopic properties selected were related to polarizability and interaction properties.